Instability and trajectories of buoyancy-driven annular disks: A numerical study

G. Corsi ,[1,*] P. G. Ledda ,[2,3,*,†] G. Vagnoli ,[3] F. Gallaire,[3] and A. De Simone [1,4,‡]
[1]*The Biorobotics Institute, Scuola Superiore Sant'Anna, 56127 Pisa, Italy*
[2]*Dipartimento di Ingegneria Civile, Ambientale e Architettura, Università degli Studi di Cagliari, 09123 Cagliari, Italy*
[3]*Laboratory of Fluid Mechanics and Instabilities, École Polytechnique Fédérale de Lausanne, CH-1015 Lausanne, Switzerland*
[4]*MathLab SISSA-International School for Advanced Studies, 34136 Trieste, Italy*

(Received 22 July 2023; accepted 14 March 2024; published 17 April 2024)

We investigate the stability of the steady vertical path and the emerging trajectories of a buoyancy-driven annular disk as the diameter of its central hole is varied. The steady and axisymmetric wake associated with the steady vertical path of the disk, for small hole diameters, behaves similarly to the one past a permeable disk, with the detachment of the vortex ring due to the bleeding flow through the hole. However, as the hole diameter increases, a second recirculating vortex ring of opposite vorticity forms at the internal edge of the annulus. A further increase in the hole size leads to the shrinking of these recirculating regions until they disappear. The flow modifications induced by the hole influence the stability features of the steady and axisymmetric flow associated with the steady vertical path. The fluid-solid coupled problem shows a nonmonotonic behavior of the critical Reynolds number for the destabilization of the steady vertical path, for low values of the disk's moment of inertia. However, for very large holes, with dimension approximately more than half of the external diameter, a marked increase of the neutral stability threshold is observed. The nature of the primary instability changes as the hole size increases, with large (small) amplitude oscillations of the trajectory at intermediate (very small and large) internal diameters. We then illustrate results obtained with fully nonlinear simulations of the time-dependent dynamics, together with a comparison of the linear stability analysis results. Falling styles, typically described as steady, hula-hoop, fluttering, chaotic, and tumbling, are shown to emerge as attractors for the nonlinear dynamics of the coupled fluid-structure system. The presence of a central hole does not always reduce the falling Reynolds number, and it may cause the transition from tumbling towards fluttering, from fluttering to hula-hoop, and from hula-hoop to steady, hence promoting trajectories with smaller lateral deviations from the vertical path. The observed trajectories and patterns agree well with linear stability analysis results, in the vicinity of the threshold of instability.

DOI: 10.1103/PhysRevFluids.9.043907

I. INTRODUCTION

Buoyancy-driven motions of bodies in a viscous fluid are a problem of interest in many engineering and scientific disciplines (cf. Ref. [1] for an extensive review). These include seed dispersal

*These authors contributed equally to this work.
†Corresponding author: piergiuseppe.ledda@unica.it
‡antonio.desimone@santannapisa.it

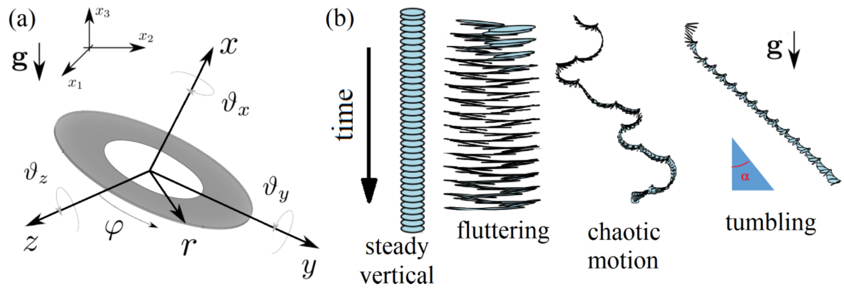

FIG. 1. (a) Sketch of the flow configuration with the employed coordinate systems. (b) Some falling style of thin disks. The falling mode has a direct impact on the lateral distance R covered, which vanishes in the case of steady vertical fall while it scales like $R \approx H_i \tan\alpha$, where H_i is the falling height, in the case of the tumbling mode.

and the unpowered flight of bio-inspired artifacts. Mazzolai *et al.* [2,3] proposed applications to environmental sensing in remote areas through biodegradable sensors which are released by drones that mimic the dispersal strategies of natural seeds. Understanding the free-fall dynamics and trajectories is crucial for planning the effective deployment of these sensors.

Nontrivial falling or rising paths stem from the interaction between the buoyancy-driven object and the surrounding fluid, as in the case of free-falling paper sheets [4–6]. Objects falling (or rising) under gravity in a fluid medium may follow complex and even chaotic trajectories depending on their geometry, the ratio of densities between the body and the surrounding fluid, and the fluid viscosity. The governing equations for this fluid-structure interaction problem are well-known [7]. In the case of a rigid body, they consist of the nonlinear equations of rigid-body dynamics, coupled with the nonlinear Navier-Stokes equations for the viscous dynamics of the surrounding fluid. The nonlinearity of this system leads to highly nontrivial behavior. Even for the case of an axially symmetric object falling along its axis of symmetry, these include instability of the straight vertical path and chaotic motions. Thin disks, which are one of the simplest three-dimensional shapes exhibiting nonstraight descent paths, have been the subject of extensive experimental and numerical research [6,8,9]. Several descent modes have been observed, e.g., steady vertical path, flutter, hula-hoop, tumbling, and chaotic. The latter represents a mix of different descent modes with the system chaotically switching between them; see Fig. 1. At least in the case of thin disks, these descent modes can be mapped onto regions of a two-dimensional parameter space consisting of the disk's dimensionless moment of inertia and the ratio of the flow's inertial-to-viscous forces, summarized by the Reynolds number associated with the average free-fall vertical velocity.

Linear stability analysis can be employed to understand the departure of the trajectory from the vertical one; see, e.g., Fabre *et al.* [10] and Assemat *et al.* [11] for two-dimensional plates. The departure from the steady vertical path of a buoyancy-driven disk was rationalized by Tchoufag *et al.* [12] via a linear stability analysis with respect to azimuthal perturbations of the steady and axisymmetric flow associated with the vertical path. The authors identified several unstable modes and found a threshold beyond which the steady vertical trajectory is unstable, depending on the disk's dimensionless moment of inertia and on the Reynolds number, with a very good agreement with the nonlinear simulation results of Auguste *et al.* [9].

With the aim of tailoring flow patterns, in the case of fixed objects, and trajectories, in the case of gravity-driven free-falling objects or buoyancy-driven bodies, local geometrical modifications of the body have been thoroughly investigated, notably in the category of permeable objects. The idea that the flow through internal holes and pores may have a strong impact in promoting the stability of falling modes has been confirmed for both natural and artificial systems [13–21]. It has been established that the structure of the flows generated by internal pores and holes plays a key role in stabilizing the steady descent mode of seeds dispersed through bristly, porous appendages;

see, e.g., the separated vortex ring developing in the wake past dandelion seeds in stable flight [14]. Internal porosity may also stabilize flows past fixed objects by suppressing wake instabilities such as periodic vortex shedding (von Karman street vortices [15,22–24]) or the onset of nonaxisymmetric and unsteady wakes past axisymmetric objects [17,25]. Permeable structures not only promote wake modifications and their stabilization for fixed bodies, but they also modify the falling trajectories in the case of buoyancy-driven objects. Vagnoli *et al.* [26] performed a linear stability analysis on the instability of the steady vertical path of permeable thin disks, highlighting the selection of specific modes depending on the permeability and, for large enough permeability, the stabilization of the steady vertical path.

The permeable body model relies on the fact that geometrical modifications are characterized by a distinct length scale, much smaller than the characteristic size of the object [27–29]. Macroscopic, internal holes may also lead to stabilization effects similar to the ones observed in biological flows related to seed dispersal. Contrary to the case of microscopic porosity, however, macroscopic holes lead to flows with marked spatial heterogeneities, and they need the complete representation of the geometry of the buoyancy-driven body. In the simple case of thin disks, here considered as a prototype of a falling object with relatively simple geometry, already a single internal hole introduces new richness in the observed behavior: annular disks have different wakes that affect the stability of the descent modes, typically delaying the occurrence of instabilities [30–34]. Vincent *et al.* [31] showed that the presence of the hole promotes a transition from tumbling to fluttering motions, which in turn induces a more vertical falling trajectory. The authors related this behavior to the decrease of the vorticity in the wake, associated with a decrease of the falling velocity because of the weight reduction.

Motivated by the arguments above, in what follows we report on the free-fall dynamics of a thin disk with a central hole, which has been selected as a benchmark test case for the study of different falling styles of biological and bio-inspired seeds and how their falling behavior may be affected by the flow patterns induced by the presence of geometric features such as bristles, pores, and holes, of macroscopic size. In particular, we consider a range of Reynolds numbers consistent with those arising in the free-fall, in air, of thin disks of a few centimeters in size, thickness of a few millimeters, and effective material density up to 100 $\mathrm{kg/m^3}$ (e.g., corrugated cardboard or porous 3D-printed material for environmental sensing applications [2,3]). A first estimate, obtained assuming a steady equilibrium between gravity force and aerodynamic drag, leads to Reynolds numbers in the range of $100 < \mathrm{Re} < 2000$. The aim of this work is to give a coherent and systematic study of the effects of the hole in a buoyancy-driven disk through the synergy of linear stability analysis and nonlinear dynamics simulations. In spite of the simplifications arising from the axial symmetry of the system, understanding the mechanisms explaining the observed trajectories requires varying systematically, and over large ranges, the values of four nondimensional parameters: the thickness over outer diameter ratio (ε), the inner over outer diameter ratio (δ), the reduced moment of inertia ($\mathscr{I}^*$), and the Reynolds number (Re). The paper is organized as follows: Section II presents the problem formulations and their numerical implementation; Sec. III studies the flow past an annular disk falling or rising with a vertical steady trajectory; subsequently, Sec. IV is devoted to the linear stability analysis of such a trajectory and to the identification of thresholds for the instability and of the emerging modes; Sec. V shows results of nonlinear simulations compared against the linear stability analysis results.

II. PROBLEM FORMULATION

A. Nonlinear equations

In this section, we present the equations governing the free-fall or rise of a buoyancy-driven annular disk of density ρ_s and thickness h. The internal and external diameters are denoted as d and D, respectively, and the volume of the disk as $\mathscr{V}$. The annular disk is immersed in a viscous fluid of constant viscosity μ and density ρ. We denote with $\bar{\boldsymbol{v}}(\bar{t})$ and $\bar{\boldsymbol{\Omega}}(\bar{t})$ the translational and rotational velocities of the body during its trajectory, respectively. We introduce a fixed Cartesian frame $(\bar{x}_1, \bar{x}_2, \bar{x}_3)$. With respect to this fixed reference frame, we introduce relative coordinate systems rotating with the disk. In particular, we employ a Cartesian reference frame $(\bar{x}, \bar{y}, \bar{z})$ for Newton's equations, and cylindrical coordinates $(\bar{x}, \bar{r}, \bar{\theta})$ for the incompressible Navier-Stokes equations for the flow dynamics (see Fig. 1). The $\bar{x}$-direction, common to both coordinate systems, is aligned along the disk axis. Following Tchoufag *et al.* [12], the flow equations are written in terms of absolute velocity. Dropping bars for nondimensional variables, the dimensional equations are nondimensionalized with the falling velocity U, the disk external diameter D, and the characteristic time D/U, leading to [12]

$$
\begin{aligned}
&\nabla \cdot \boldsymbol{u} = \mathbf{0},\\
&\frac{\partial \boldsymbol{u}}{\partial t} + (\boldsymbol{u} - \boldsymbol{w}) \cdot \nabla \boldsymbol{u} + \boldsymbol{\Omega} \times \boldsymbol{u} = -\nabla p + \frac{1}{\mathrm{Re}} \nabla^2 \boldsymbol{u},\\
&M \frac{\mathrm{d}\boldsymbol{v}}{\mathrm{d}t} + M \boldsymbol{\Omega} \times \boldsymbol{v} = (M - \rho \mathscr{V}) \boldsymbol{g} + \int_{\Gamma_d} \Sigma \boldsymbol{n} \mathrm{d}\Gamma,\\
&\mathscr{I} \cdot \frac{\mathrm{d}\boldsymbol{\Omega}}{\mathrm{d}t} + \boldsymbol{\Omega} \times (\mathscr{I} \boldsymbol{\Omega}) = \int_{\Gamma_d} \boldsymbol{r} \times (\Sigma \boldsymbol{n}) \mathrm{d}\Gamma, \quad \Sigma = -p\mathbf{I} + \frac{1}{\mathrm{Re}} (\nabla \boldsymbol{u} + \nabla \boldsymbol{u}^T),
\end{aligned} \tag{1}
$$

where Σ is the nondimensional stress tensor, $\boldsymbol{w} = \boldsymbol{v} + \boldsymbol{\Omega} \times \mathbf{r}$, $\mathrm{Re} = \rho U D/\mu$ is the Reynolds number, $M = \rho_s \mathscr{V}/(\rho D^3)$ is the nondimensional mass of the disk, and $\mathscr{I} = \bar{\mathscr{I}}/(\rho D^5)$ is the nondimensional inertia tensor; for an annular disk, the nonzero diagonal components of its dimensional counterpart $\bar{\mathscr{I}}$ read

$$
\bar{\mathscr{I}}_{xx} = \tfrac{1}{8} \bar{M} D^2 (1 + \delta^2), \quad \bar{\mathscr{I}}_{yy} = \bar{\mathscr{I}}_{zz} = \tfrac{1}{16} \bar{M} D^2 \left(1 + \delta^2 + \tfrac{4}{3} \varepsilon^2\right), \tag{2}
$$

where $\varepsilon = h/D$ and $\delta = d/D$ are the nondimensional thickness and internal radius, respectively, while the dimensional mass reads $\bar{M} = \frac{\pi}{4} \rho_s (D^2 - d^2) h$. The off-diagonal terms are identically zero. The problem is closed with the far-field condition $\boldsymbol{u} = \mathbf{0}$ and the zero relative velocity Dirichlet boundary condition at the disk $\boldsymbol{u} = \boldsymbol{w}$.

B. Steady vertical path

The velocity and pressure fields $[\boldsymbol{U}, P]$ associated with the steady vertical path of constant vertical velocity $\boldsymbol{V} = -\mathbf{e}_x$ and zero angular velocity, with the disk axis aligned with the flow, satisfy the steady and axisymmetric Navier-Stokes equations:

$$
\nabla \cdot \boldsymbol{U} = 0, \quad (\boldsymbol{U} + \mathbf{e}_x) \cdot \nabla \boldsymbol{U} + \nabla P - \frac{1}{\mathrm{Re}} \nabla^2 \boldsymbol{U} = \mathbf{0}, \quad \lim_{\|\mathbf{r}\| \to \infty} \boldsymbol{U} = \mathbf{0}, \tag{3}
$$

with $\boldsymbol{U} = -\boldsymbol{e}_x$ at the disk walls and symmetry conditions at $r = 0$ [12]. The problem is formally analogous to the fixed-body case if the relative velocity $\boldsymbol{U} + \mathbf{e}_x$ is considered. Besides, Newton's equations reduce to the equilibrium between nondimensional gravity and drag $D_0 = \int_{\Gamma_{\mathrm{int}}} \Sigma(\boldsymbol{U}, P) \mathrm{d}\Gamma_{\mathrm{int}}$ along the vertical direction. In this nondimensionalization, once the thickness ε and the internal radius δ are fixed, the falling Reynolds number Re is the only nondimensional parameter that describes the steady vertical path.

The flow equations are solved in a rectangular domain corresponding to a section $\varphi = \mathrm{const}$, for the coordinates (x, r) (see Fig. 1). We impose zero velocity at the boundary located at $x = x_{-\infty}$ and $r = r_{\infty}$, and the free-stress condition at $x = x_{+\infty}$, together with the zero relative velocity Dirichlet condition at the disk. On the axis, we impose the symmetry condition $u_r = 0$ [12]. The numerical implementation of the weak form of the various equations is performed in COMSOL MULTIPHYSICS, with Taylor-Hood elements for the velocity and pressure fields. The numerical details are reported in Appendix A.

C. Linear stability analysis of the steady vertical path

We study the linear stability of the steady and axisymmetric flow associated with the steady vertical falling or rising path of the disk along its symmetry axis. The following decomposition is introduced ($\varsigma \ll 1$):

$$[\boldsymbol{u}, p] = [\boldsymbol{U}(x, r), P(x, r)] + \varsigma[\boldsymbol{u}'(x, r, \theta), p'(x, r, \theta)],$$
$$\boldsymbol{v}(t) = -\mathbf{e}_x + \varsigma \boldsymbol{v}'(t), \quad \boldsymbol{\Omega}(t) = \varsigma \boldsymbol{\omega}'(t). \tag{4}$$

Upon substitution in Eq. (1), the steady and axisymmetric Navier-Stokes equations described in the previous section and satisfied by the field $(\boldsymbol{U}, P)$ are recovered at order $O(1)$, while at $O(\varsigma)$ the equations for the linearized dynamics are obtained [12]. For small angles, $\boldsymbol{g} = -g\mathbf{e}_x + \varsigma g(\vartheta_y \mathbf{e}_z - \vartheta_z \mathbf{e}_y)$, where we introduced the components of the vector $\boldsymbol{\Theta}(t) = \varsigma \boldsymbol{\vartheta}'(t) = \varsigma(\vartheta_x, \vartheta_y, \vartheta_z)$, whose components are the inclination angles of the reference frame that rotates with the disk with respect to the fixed reference of the steady vertical path. We consider a normal mode expansion of the perturbation of azimuthal wave number m and complex growth rate $\sigma \in \mathbb{C}$:

$$\boldsymbol{u}'(x, r, t) = \hat{\boldsymbol{u}}(x, r)\mathrm{e}^{\mathrm{i}m\varphi + \sigma t}, \quad p'(x, \boldsymbol{r}, t) = \hat{p}(x, r)\mathrm{e}^{\mathrm{i}m\varphi + \sigma t},$$
$$\boldsymbol{v}(t) = \hat{\boldsymbol{v}}\mathrm{e}^{\sigma t}, \quad \boldsymbol{\omega}'(t) = \hat{\boldsymbol{\omega}}\mathrm{e}^{\sigma t}, \quad \boldsymbol{\vartheta}'(t) = \hat{\boldsymbol{\vartheta}}\mathrm{e}^{\sigma t}. \tag{5}$$

Tchoufag *et al.* [12] showed that modes with $m = 0$ are stable. Also, modes with $|m| > 2$ do not influence the path's linear instability since the integral contribution in Newton's equations is zero, and thus the wake dynamics is decoupled from that of the disk. In the following, we investigate the modifications of the instabilities with azimuthal wave number $m = \pm 1$. Right-handed helices are obtained for $m = 1$ and $\mathrm{Im}(\sigma) > 0$, while left-handed helices are characterized by $m = -1$ and $\mathrm{Im}(\sigma) > 0$. Linear stability analysis admits both types of solutions, and the superposition of helices of opposite sign and the same amplitude leads to planar zigzagging paths [12]. The assumption $m = \pm 1$ implies, by symmetry, $\hat{v}_x = \hat{\vartheta}_x = 0$. The projections of the linearized Newton's equations [obtained at order $O(\varsigma)$] along y and z are combined in one single equation through the $U(1)$ transformation ($\hat{v}_\pm = \hat{v}_y \mp \mathrm{i}\hat{v}_z$, $\hat{\omega}_\pm = \hat{\omega}_z \pm \mathrm{i}\hat{\omega}_y$, $\hat{\vartheta}_\pm = \hat{\vartheta}_z \pm \mathrm{i}\hat{\vartheta}_y$) for $m = \pm 1$ [7]. The linearized Newton's equations for the perturbation, upon introduction of the normal mode expansion and of the $U(1)$ transformation, read

$$M\sigma \hat{v}_\pm = \pm M\hat{\omega}_\pm \pm D_0 \hat{\vartheta}_\pm + 2\pi \int_{\Gamma_{\mathrm{int}}} \left[\frac{1}{2}\left(-\hat{p} + \frac{2}{\mathrm{Re}}\frac{\partial \hat{u}_r}{\partial r}\right)n_r \mathrm{d}x + \frac{1}{\mathrm{Re}}\left(\frac{\partial \hat{u}_x}{\partial r} + \frac{\partial \hat{u}_r}{\partial x}\right)n_x r\mathrm{d}r\right]$$
$$\mp \frac{2i\pi}{\mathrm{Re}} \int_{\Gamma_{\mathrm{int}}} \left[\frac{1}{2}\left(\frac{\partial \hat{u}_\varphi}{\partial r} - \frac{\hat{u}_\varphi}{r} \pm \frac{i\hat{u}}{r}\right)n_r \mathrm{d}x + \left(\frac{\partial \hat{u}_\varphi}{\partial x} \pm \frac{i\hat{u}_x}{r}\right)n_x r\mathrm{d}r\right], \tag{6}$$

$$\sigma \mathscr{I}^* \hat{\omega}_\pm = -2\pi \int_{\Gamma_{\mathrm{int}}} r\left[\left(-\hat{p} + \frac{2}{\mathrm{Re}}\frac{\partial \hat{u}_x}{\partial x}\right)n_x r\mathrm{d}r + \frac{1}{2\mathrm{Re}}\left(\frac{\partial \hat{u}_x}{\partial r} + \frac{\partial \hat{u}_r}{\partial x}\right)n_r \mathrm{d}x\right]$$
$$+ 2\pi \int_{\Gamma_{\mathrm{int}}} x\left[\frac{1}{2}\left(-\hat{p} + \frac{2}{\mathrm{Re}}\frac{\partial \hat{u}_r}{\partial r}\right)n_r \mathrm{d}x + \frac{1}{\mathrm{Re}}\left(\frac{\partial \hat{u}_x}{\partial r} + \frac{\partial \hat{u}_r}{\partial x}\right)n_x r\mathrm{d}r\right]$$
$$\mp i\pi \int_{\Gamma_{\mathrm{int}}} x\left[\frac{1}{2\,\mathrm{Re}}\left(\frac{\partial \hat{u}_\varphi}{\partial r} - \frac{\hat{u}_\varphi}{r} \pm \frac{i\hat{u}_r}{r}\right)n_r \mathrm{d}x + \frac{1}{\mathrm{Re}}\left(\frac{\partial \hat{u}_\varphi}{\partial x} \pm \frac{i\hat{u}_x}{r}\right)n_x r\mathrm{d}r\right] \tag{7}$$

$$\sigma \hat{\vartheta}_\pm = \hat{\omega}_\pm, \tag{8}$$

where $\mathscr{I}^* = \mathscr{I}_{yy} = \mathscr{I}_{zz}$ and $M = 16\mathscr{I}^*/[1 + \delta^2 + (4/3)\varepsilon^2]$, i.e., M is slaved to $\mathscr{I}^*$ because of geometry. Coupled with the continuity equation for the perturbation $\nabla_\pm \cdot \hat{\boldsymbol{u}} = \boldsymbol{0}$, the linearized

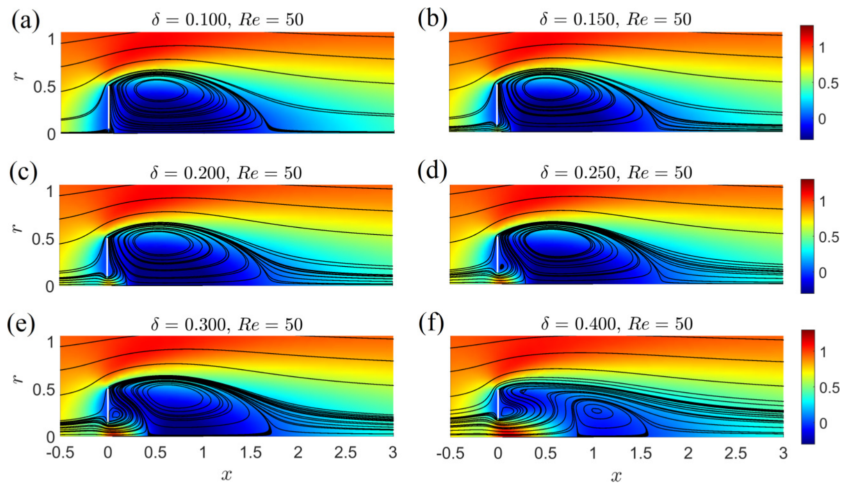

FIG. 2. $\varepsilon = 10^{-3}$. Streamlines and isocontours of the streamwise relative velocity, for increasing values of δ and fixed Re = 50.

Navier-Stokes equations read

$$\begin{aligned} &\sigma\hat{\boldsymbol{u}} + \hat{\boldsymbol{u}}\cdot\nabla\boldsymbol{U} + (\boldsymbol{U} + \mathbf{e}_x)\cdot\nabla_{\pm}\hat{\boldsymbol{u}} \\ &\quad = -\nabla_{\pm}\hat{p} + \frac{1}{\text{Re}}\nabla_{\pm}^2\hat{\boldsymbol{u}} + \frac{1}{2}\left(\frac{\partial\boldsymbol{U}}{\partial r} \pm \frac{iU_r}{r}\mathbf{e}_{\varphi}\right)\hat{v}_{\pm} \\ &\qquad + \left\{\mp\frac{1}{2}\left[r\frac{\partial\boldsymbol{U}}{\partial x} - (U_x\mathbf{e}_r + U_r\mathbf{e}_x)\right] \pm \frac{1}{2}x\frac{\partial\boldsymbol{U}}{\partial r} \pm \frac{1}{2}i\left[x\frac{U_r}{r} - U_x\right]\mathbf{e}_{\varphi}\right\}\hat{\omega}_{\pm}, \end{aligned} \tag{9}$$

where $\nabla_{\pm}$ is the nabla operator upon introduction of the normal mode expansion; see Tchoufag *et al.* [12] for the complete expression. The linearized Navier-Stokes equations are closed with zero velocity conditions on the inlet and lateral boundary, zero stress at the outlet boundary, zero relative velocity on the disk surface, and suitable symmetry conditions for $m = 1$ modes on the axis; see, e.g., Meliga *et al.* [35]. The resulting problem is an eigenvalue problem of the form $\mathbf{A}\hat{\mathbf{q}} = \sigma\mathbf{B}\hat{\mathbf{q}}$. The linear stability equations are solved in the same rectangular domain corresponding to $\varphi = \text{const}$ (see Fig. 1). Newton's equations are implemented as ODE problems, with integrals at the disk surface discretized through a fourth-order Gaussian quadrature rule. Upon solution of the steady and axisymmetric problem for the baseflow $(\boldsymbol{U}, P)$ for a specific combination of $(\text{Re}, \delta, \varepsilon)$, the stability analysis is performed for the same values of these parameters and for different values of the disk moment of inertia $\mathscr{I}^*$. To this end, we employ the COMSOL built-in eigenvalue solver based on the ARPACK Library. The algorithm was validated against the stability results for a solid disk with thickness 10^{-4} of [12], in the case $\delta = 0$. We performed a mesh independence analysis, as reported in Appendix A. We now study the steady vertical path and its stability for a very thin disk with $\varepsilon = 10^{-3}$. The effect of varying the thickness is extensively discussed in the Supplemental Material [36].

III. STEADY AND AXISYMMETRIC FLOW ASSOCIATED WITH THE VERTICAL PATH

The steady and axisymmetric solution associated with the steady vertical path of a buoyancy-driven annular disk, in the absence of the hole (here denoted as a *full* disk), presents a toroidal recirculation region completely attached to the body. The presence of a hole progressively modifies this picture, as shown in Fig. 2, for fixed Re = 50, with a downstream displacement of the recirculation region, which bends and remains attached to the disk. The velocity through the hole

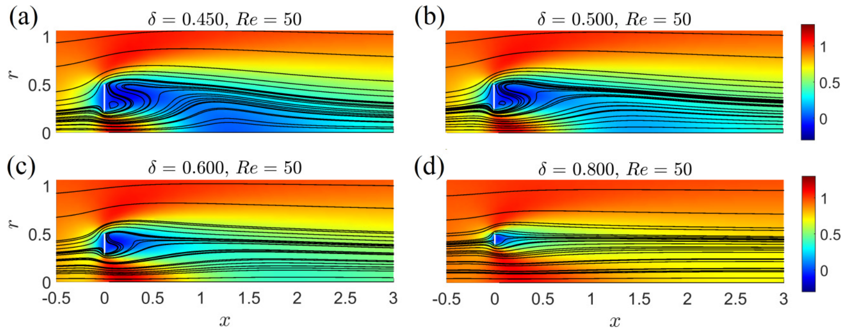

FIG. 3. $\varepsilon = 10^{-3}$. Streamlines and isocontours of the streamwise relative velocity, for increasing values of δ and fixed Re = 50.

increases and reaches values of the same order as that of the free-stream. In parallel, a second recirculation region of opposite vorticity (*negative* vorticity, in contrast with the *positive* sign of the first recirculation) forms. At $\delta = 0.4$, a sudden transition of the flow pattern is observed. The flow is now characterized by a recirculation region completely detached from the body, and the recirculation region of negative vorticity now dominates the wake dynamics in the vicinity of the disk. The region of large velocity close to the axis becomes larger and the bleeding effect remains present further downstream. As shown in Fig. 3, at $\delta = 0.45$, the first recirculation region eventually disappears, even if a region of low velocity (*defect*) is observed downstream of the body. For $\delta = 0.5$, a small detached recirculation is also observed in the vicinity of the disk edge. At the same time, the recirculation region of negative vorticity decreases its size and, for $\delta = 0.6$, the flow streamlines are almost straight with a region of small velocity restrained in the near wake of the annulus.

In summary, the presence of a hole of increasing size, for fixed Re, leads to the formation of a central jet of large velocity. This jet tends to displace downstream the main recirculation region. When the hole and the associated velocity are large enough, the flow separates at the inner edge, and a second recirculation region appears. This flow separation induces a relative velocity that pushes the fluid upstream, competing with the jet effect, which instead moves the main recirculation downstream. When the internal radius is approximately half of the external one, the main recirculation detaches, becomes smaller, and disappears. However, a small recirculation induced by the internal flow separation is still observed. Eventually, these recirculations become smaller and disappear as the internal radius approaches the external one.

The effect of the Reynolds number is reported in Fig. 4. In the case $\delta = 0.25$, an increase of Re leads to an increase of the size of the recirculation region, which almost doubles its length from Re = 25 to 100. Also, the small recirculation caused by the separation at the internal radius increases its size. The case $\delta = 0.4$ shows a recirculation region completely detached from the body already at Re = 25. At Re = 100, a third recirculation region of positive vorticity forms, in the vicinity of the disk edge. For $\delta = 0.5$ and small Re, only the recirculation induced by the separation at the internal radius is present, with a wake defect whose minimum is located at $x \approx 1$. An increase in the Reynolds number leads to the formation of a third recirculation region of positive vorticity in the vicinity of the disk edge.

The behavior of the first recirculation region can be described by two quantities, its distance X_R from the rear of the disk, and its length L_R, measured on the axis. Figure 5 shows the isocontours of (a) L_R and (b) X_R in the (δ, Re) plane.

The distance X_R of the axial separation point closing the first recirculation region progressively increases with δ [Fig. 5(b)]. For $\delta \sim 0.4$, the recirculation length presents a nonmonotonic behavior with Re, i.e., it increases, reaches a maximum, and decreases until it disappears. We identify a critical value of $\delta = 0.45$, in the considered range of parameters, beyond which the first recirculation

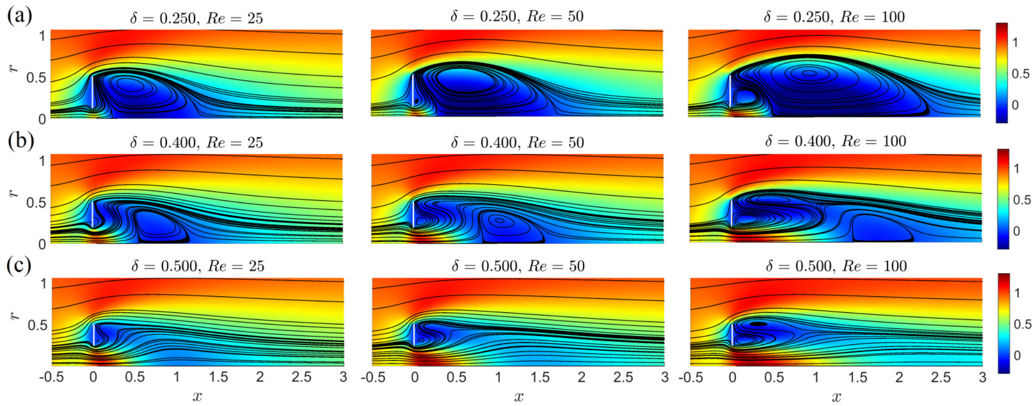

FIG. 4. $\varepsilon = 10^{-3}$. Streamlines and isocontours of the axial relative velocity, for increasing values of δ (from the top to the bottom) and increasing values of $\mathrm{Re} = 25,\ 50,\ 100$ (from the left to the right).

is absent. The flow topology influences also the values of the nondimensional drag D_0, an essential quantity to define the falling velocity and thus the stability of the falling trajectory. The isocontours of D_0 in the (δ, Re) plane are reported in Fig. 5(c). The drag monotonically decreases with Re while it presents a nonmonotonic behavior with δ, characterized by an initial increase followed by a rapid decrease for $\delta > 0.4$, approximately. The peak becomes steeper as Re increases. This behavior is very similar to the permeable disk case [13,14,26], where a similar drag peak is observed, close to the critical value of permeability beyond which there is no recirculation region. We can infer the origin of this mechanism by observing the bleeding flow from the central hole. As shown in Figs. 2–4, an increase in δ within the range $0 < \delta < 0.4$–0.5 leads to a progressive increase of the intensity of the bleeding flow through the hole. However, increasing δ beyond 0.4, the peak in the streamwise velocity decreases, and, more importantly, the difference between the upstream and downstream velocity through the hole decreases. Since $\Delta p \sim \Delta u_x^2$, the maximum pressure difference occurs for approximately $\delta = 0.4$, whereas beyond this value of δ, the pressure drop decreases. This behavior is due to the competition between the bleeding flow and the aerodynamic flow around the whole object. As the hole size increases, more flow passes through the hole, thus leading to a more intense bleeding flow (and pressure drop) when the hole is small. However, as the hole becomes larger, the confinement effect decreases, thus promoting streamlines more aligned with the asymptotic flow, with smaller peak velocities and a subsequent decrease in the pressure drop across the hole. Since the pressure drop can be reasonably correlated to the drag for a bluff body, the competition of these two effects leads to the observed peak in the drag coefficient.

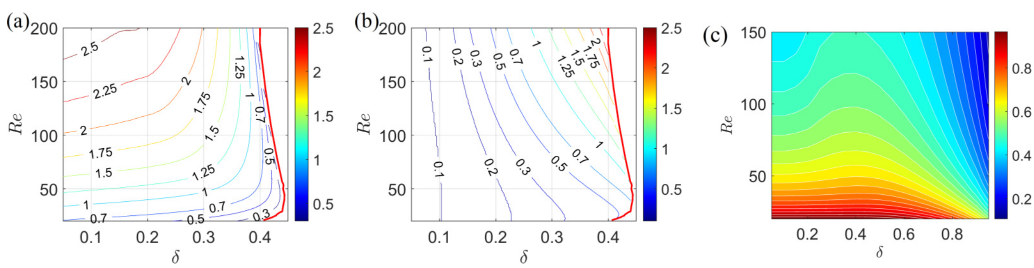

FIG. 5. $\varepsilon = 10^{-3}$. Isocontours of (a) length of the recirculation region L_R and (b) its distance from disk X_R, obtained by finding the zeros of the axial relative velocity on the axis, as functions of Re and δ. (c) Isocontours of the nondimensional drag D_0 as a function of Re and δ.

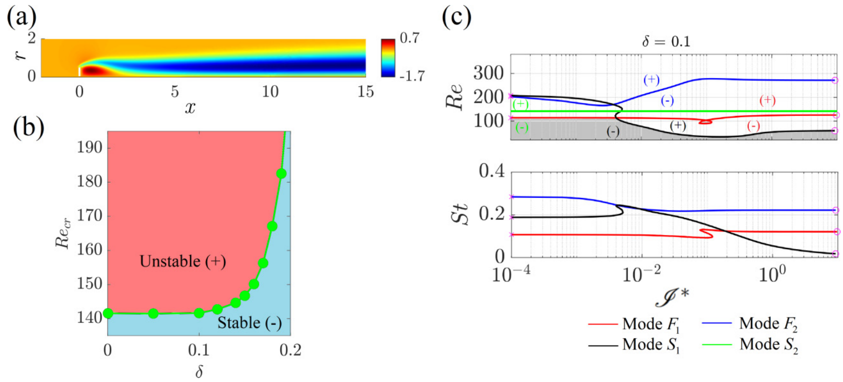

FIG. 6. (a), (b) Nonoscillatory mode. (a) Real part of the streamwise component of the velocity eigenvector, rescaled with $\vartheta_{\pm}$, for Re = 144, $\delta = 0.1$, and $\varepsilon = 10^{-3}$. The imaginary part is identically zero. (b) Critical Reynolds number of the nonoscillatory mode as a function of δ. (c) Marginal stability curves in the ($\mathcal{I}^*$, Re) plane, for $\delta = 0.1$ and $\varepsilon = 10^{-3}$. The (+) and (−) help identify the regions with positive and negative real part of the eigenvalues, and the symbols *o* and *x* connect the neutral curves to the corresponding Strouhal number ones (on the bottom). The gray regions identify where the steady vertical path is linearly stable with respect to azimuthal perturbations.

In summary, the variety of observed flow topologies is related to the bleeding effect through the hole and the competition between the separation at the internal and external edges. An increase in the Reynolds number leads to an increase of the bleeding effect through the hole and of the strength of the separation at the internal disk edge. The flow features with δ and Re resemble those of the wake past a permeable body [13,15]. The detachment from the body of the first recirculation due to bleed in through the hole appears very similar to the one induced by an increasing permeability. However, for small δ, this detachment is not complete since the bubble remains attached to the disk tip. In opposition to the permeable case, the strength of the flow separation is not directly correlated to an increase of the bleeding flow. The complete separation of the first recirculation is instead related to the more intense flow separation at the disk internal edge, which at some point involves the whole annulus. Due to the competition between the two flow separations, an increase in the Reynolds number leads to a nonmonotonic behavior of the length recirculation region. In the next section, we identify the conditions that lead to the departure from the described base flow through the linear stability analysis framework presented in Sec. II.

IV. FLUID-STRUCTURE INTERACTION: INSTABILITY OF THE STEADY VERTICAL PATH

A. The nonoscillatory mode

In the full disk case, several modes are known [12] to become unstable in the (Re, $\mathcal{I}^*$) plane. Three of them are oscillatory, whereas one is independent of inertia and nonoscillatory [12]. We begin by considering the effect of δ on the nonoscillatory mode. Its spatial structure [Fig. 6(a)] is characterized by a wake with a real part of constant sign that propagates downstream, while the imaginary part is identically zero, once rescaled with $\hat{\vartheta}_{\pm}$. Note that this rescaling allows for identifying in the real and imaginary parts two instants of the trajectory, i.e., the ones with maximum inclinations along the *y* and *z* directions [12]. The nonoscillatory mode is very similar to the steady one associated with the pure aerodynamic problem; see the Supplemental Material [36]. This structure was labeled by [12] as a sign preserving type (SPT) structure, in contrast with a sign alternating type (SAT structures), which instead are spatial distributions very similar to the oscillatory modes of the fixed case. The SPT/SAT structures here described result from the bifurcation of the steady and axisymmetric (SA) wake. In the fixed-body problem, the SA wake undergoes two bifurcations often labeled as SS (steady state) and SW (standing wave), as thoroughly described by Fabre *et al.* [37] and Meliga *et al.* [38]. The SPT and SAT structures can be seen as the fluid-structure interaction counterparts of the SS and SW bifurcations, respectively, since they both stem from the instability of the steady and axisymmetric wake past a fixed disk. The combination or dominance of SPT or SAT structures in the real and imaginary parts of the modes, rescaled with $\hat{\vartheta}_{\pm}$, help in qualitatively identifying the fluid-structure interaction or the segregation between the disk dynamics and the wake one, during one period. In the fixed-disk case, the nonoscillatory instability causes a steady shift in the wake, in the nonlinear regime. If the disk could move, this shift would make it rotate towards an inclined path. Thus, the main impact of SPT structure is altering the disk's orientation, with the wake's tilt being a result of the disk's angle. Conversely, SAT disturbances involve downstream oscillations that resemble the shedding of vortical structures, indicating that the wake's instability governs the disk's dynamics [9,12]. In the case of Fig. 6(a), a zero imaginary part means $\hat{\vartheta}_z = 0$ and thus an exponentially increasing inclination along the y direction, since the frequency is identically zero. Nonlinear effects, eventually, would lead to saturation of the trajectory with a constant inclination angle, as observed by Auguste *et al.* [9] for the full disk geometry.

The effect of δ on the neutral curve of the nonoscillatory mode is shown in Fig. 6(b). An increase in δ leads to an abrupt increase of the critical Reynolds number for the instability and reaches values larger than 200. With a good approximation, the nonoscillatory mode becomes stable for $\delta > 0.2$, in the studied range of Re.

B. The oscillatory modes

The stability of the nonoscillatory mode is not enough to ensure the overall stability of the steady vertical path since other modes may be unstable. Figure 6(c) shows the neutral curves, i.e., the locus of the zero-growth-rate, so-called marginal, eigenvalues in the (Re, $\mathscr{I}^*$) plane, for $\delta = 0.1$. These curves are built by continuation, starting from very low and very large inertia values. Each curve defines two regions in the plane, an unstable and a stable one, whose sides are denoted with a plus and a minus sign, respectively. The gray region depicts the part of the ($\mathscr{I}^*$, Re) plane in which the steady vertical path is stable, i.e., there are no eigenvalues with a positive real part. The stable region is bounded by the red and black curves, respectively, at low and large inertia. Therefore, the first instability encountered by the steady vertical path is given by oscillatory modes, in the whole range of $\mathscr{I}^*$. The presented picture of modes is very similar to the full disk case described in [12], although the considered thickness is slightly larger.

The red curve is associated with an eigenvalue that is retrieved also in the fixed case (i.e., the oscillatory one of the pure aerodynamic case) as $\mathscr{I}^* \to \infty$, and its real part and Strouhal number, defined as $\mathrm{St} = (fD)/U = \mathrm{Im}(\sigma)/(2\pi)$ (where f is the oscillation frequency in dimensional form), are weakly dependent on the disk inertia. According to [12], this curve is labeled F_1. Conversely, the eigenvalue associated with the black curve is present only in the fluid-solid coupled problem and presents large variations with $\mathscr{I}^*$ both in the real and imaginary parts. Also, the imaginary part decreases as $\mathscr{I}^{*-1/2}$, which gives a criterion to identify this mode as δ increases. This mode is labeled S_1, following [12]. The green line is associated with the nonoscillatory mode previously described and is independent of the disk inertia. This mode is labeled S_2, since it is present only in the fluid-solid coupled problem. The blue curve is associated with a mode that is identified at large Reynolds numbers also in the fixed problem, and is thus labeled F_2. We also note the presence of a loop in the black neutral curve, which defines a small island of stability in the ($\mathscr{I}^*$, Re) plane, thoroughly described in the literature [9,12,26].

The spatial distributions of the oscillatory modes are reported in Fig. 7. Mode F_1 is characterized by SAT structures, in which the imaginary part appears as a downstream shift of the real part, strongly reminiscent of the oscillatory mode of the pure aerodynamic case. Its distribution does not quantitatively change at small and large disk inertia. In nonlinear simulations [9], this mode structure was associated with strong wake oscillations, coupled with very small oscillations of the disk trajectory with respect to the vertical one. Mode S_1 [panel (b)] instead shows strong

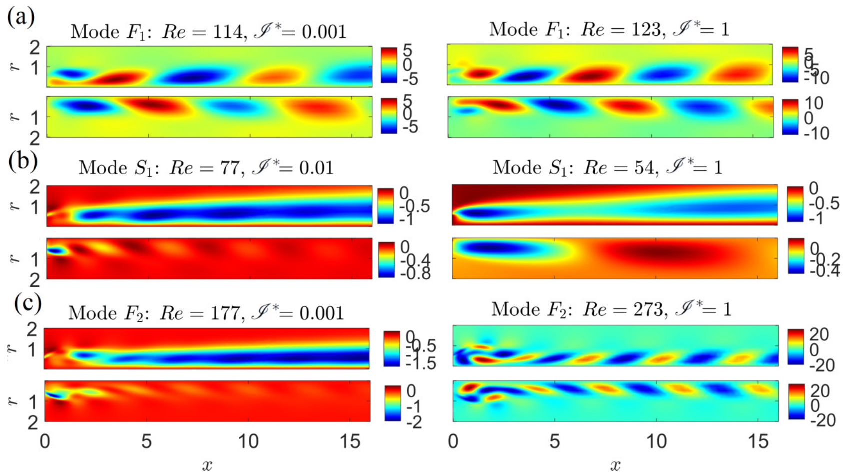

FIG. 7. $\varepsilon = 10^{-3}$ and $\delta = 0.1$. Real part of the streamwise component of the velocity eigenvector, rescaled with $\hat{\vartheta}_{\pm}$, at the marginal stability, for different modes and values of $\mathscr{I}^*$.

variations with the disk inertia. In both cases, the real part is dominated by a SPT structure, while the imaginary part shows structures of alternating sign when moving downstream. This eigenvector is thus associated with a strong fluid-solid coupling, and, in the nonlinear regime, this would ultimately lead to large-amplitude oscillations of the disk trajectory [9]. Mode F_2 [panel (c)], at low disk inertia, resembles mode S_1, with vortical structures of smaller streamwise extent. However, at large inertia, the spatial distribution is reminiscent of mode F_1, with SAT structures.

C. Effect of the disk hole

We now describe the effect of δ on the instabilities encountered by the steady vertical path. We label by continuity the modes based on their behavior at large and low inertia. Figure 8(a) shows the neutral curves for $\delta = 0.25$. The globally stable (gray) region becomes slightly larger, and, at low inertia, the overall first instability is given by mode F_2. Mode S_2 is stable in the considered range of Re, in agreement with Fig. 6. We also identify a new mode, present only at low inertia (cyan curve), which we label S_3. However, this mode becomes unstable at very large Reynolds numbers, far from the threshold of instability of the steady vertical path. An increase to $\delta = 0.27$ [panel (b)] does not lead to significant differences, although another mode present at large inertia and large Reynolds numbers, here labeled F_3, is present. At $\delta = 0.3$ [panel (c)], the F-curves abruptly move toward larger Reynolds numbers, and the primary destabilization is given by mode S_1 in the whole range of $\mathscr{I}^*$. Also, there is a large loop region associated with the restabilization of mode S_1. However, the stable (gray) region of the steady vertical path remains qualitatively the same. Therefore, the effect of the disk hole for $\delta < 0.3$ is an abrupt increase of the critical Reynolds numbers of the nonoscillatory mode S_2 and of the F-modes.

In panel (d) ($\delta = 0.4$), only modes F_2 and S_1 remain unstable, with the former only at very large Reynolds numbers. A restabilizing branch of mode S_1 is present, which defines an island of stability of the steady vertical path, with an extent similar to the case $\delta = 0.3$. For larger values of δ, also the neutral curve of mode S_1 abruptly moves at large Reynolds numbers, and, at $\delta = 0.7$ [Fig. 9(a)], the only instability present in the considered plane is given by mode S_1 and occurs at large Reynolds numbers. A further increase in $\delta = 0.8$ leads to a shift of the neutral curves toward even larger Reynolds numbers [Fig. 9(b)].

Variations in the marginal stability curves are associated with modifications of the eigenvectors at the primary instability of the steady vertical path. Figure 10 shows the marginally stable modes

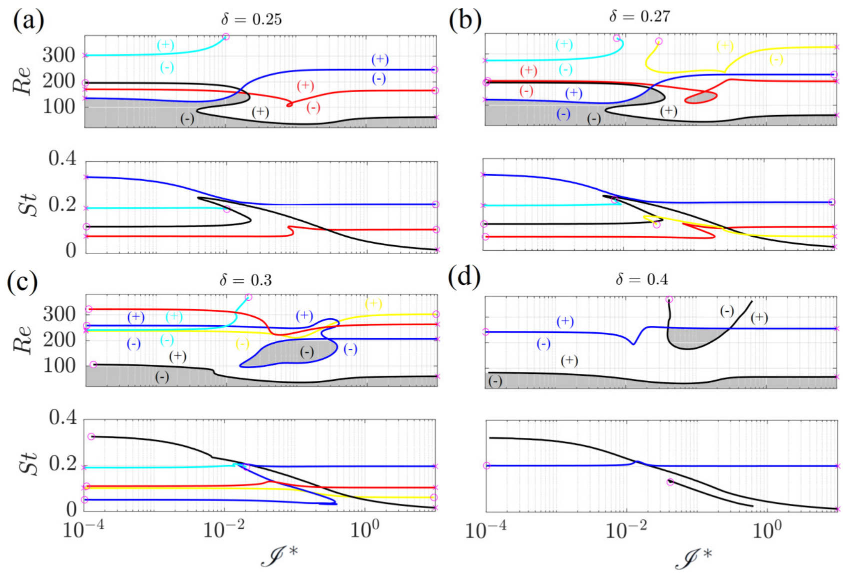

FIG. 8. Marginal stability curves in the ($\mathscr{I}^*$, Re) plane, for increasing values of δ and fixed $\varepsilon = 10^{-3}$. The (+) and (−) help identify the regions with positive and negative real part of the eigenvalues, and the symbols o and x to connect the neutral curves to the corresponding Strouhal number ones. The gray regions identify where the steady vertical path is linearly stable with respect to azimuthal perturbations.

of the steady vertical path, at the critical Reynolds number for the first instability, for fixed $\mathscr{I}^*$ and increasing size of the hole. We begin by considering $\mathscr{I}^* = 0.001$ [panel (a)]. For $\delta = 0.1$, the mode structure is analogous to the full-disk case, with structures of alternating sign. The imaginary part appears as a phase shift of the corresponding real part. At $\delta = 0.25$, the far-wake is a sign-preserving type structure, where both the real and imaginary parts are nonzero and present the opposite sign. In the vicinity of the disk, small structures of alternating sign are instead present. For $\delta = 0.4$, the pattern is very similar, although the critical Reynolds number is lower. At very large $\delta = 0.7$, the wake is dominated by structures of alternating sign, where real and imaginary parts appear phase-shifted. In panel (b), an increase in δ does not strongly modify the spatial distribution of the eigenvectors, which are characterized by a dominance of sign-preserving type structures and opposite sign between real and imaginary parts, with an exception in the close vicinity of the disk. For $\delta = 0.7$, a slight variation of the mode is observed, with a decrease of the Strouhal number associated with the instability and consequent stretching of the vortical structures along the streamwise direction.

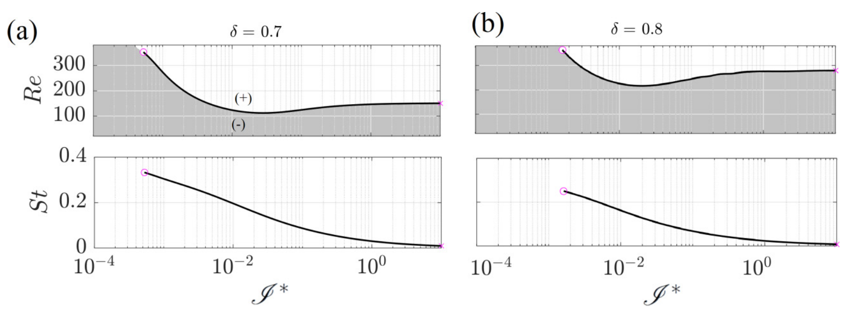

FIG. 9. Same as Fig. 8 for (a) $\delta = 0.7$ and (b) $\delta = 0.8$.

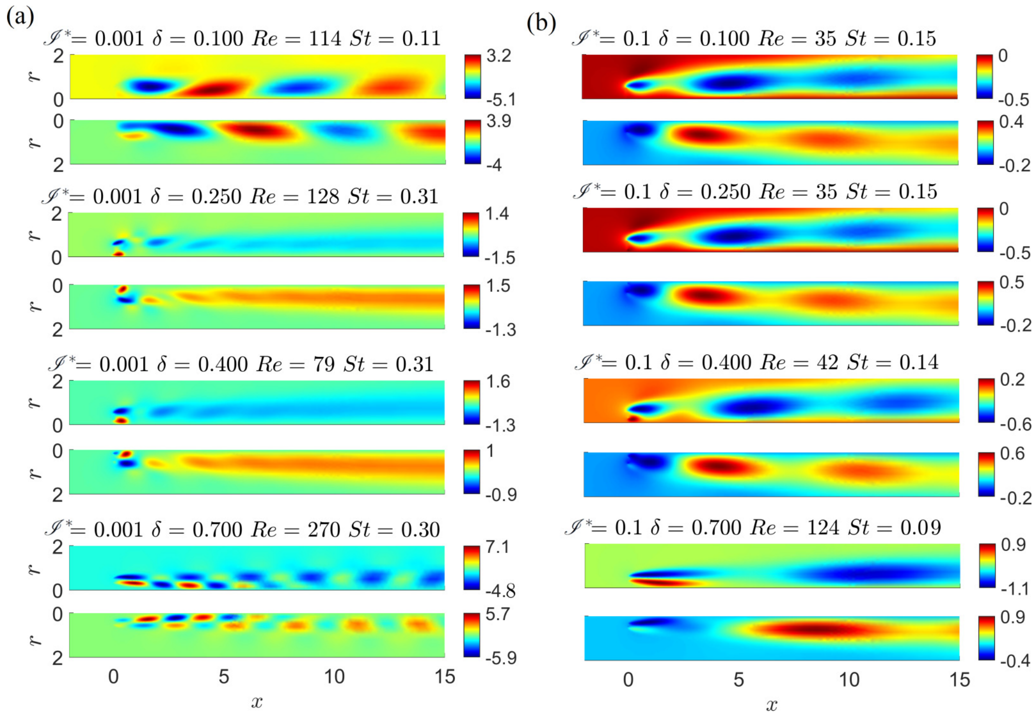

FIG. 10. $\varepsilon = 10^{-3}$. Real (on the top) and imaginary (on the bottom) parts of the streamwise component of the velocity eigenvector, rescaled with $\hat{\vartheta}_{\pm}$, for (a) $\mathscr{I}^* = 0.001$ and (b) $\mathscr{I}^* = 0.1$ and increasing values of δ, from the top to the bottom. The plotted modes are identified as the first threshold encountered by the steady vertical path as Reynolds increases, for fixed δ.

At large values of $\mathscr{I}^*$, the wake structure of the unstable mode is not strongly modified by the increase of the hole diameter. The differences become substantial only when very large values of the hole radius are considered. Conversely, at low disk inertia the size of the hole modifies the instability thresholds and the structures of the modes. The critical Reynolds number for the instability presents a nonmonotonic behavior, with an initial decrease followed by an abrupt increase. At low values of δ, the mode is reminiscent of the full-disk case, and it would ultimately lead to low-amplitude oscillations of the disk, in the nonlinear regime [12]. For larger values of δ, structures of constant sign are instead observed, which can be associated with large-amplitude disk oscillations. However, at large $\delta = 0.7$, a regime with small oscillations of the disk is recovered, with a much faster frequency compared to the full-disk case.

The effect of a hole is similar to an increase of permeability; see Vagnoli *et al.* [26]. Initially, modes characterized by large wake oscillations are stabilized, followed by those that are dominated by the disk dynamics (with a weak effect on wake oscillations). However, the permeability-induced restabilization at large Reynolds number [26] is absent in the annular disk case. We observe only a progressive increase of the marginal stability thresholds, without restabilizing branches, at least in the considered range of Re. In the following, we relate the stability observations with nonlinear simulations of falling annular disks in the range $0.001 < \mathscr{I}^* < 0.1$.

V. FALLING STYLES AS ATTRACTORS FOR THE NONLINEAR DYNAMICS: RESULTS OF FULLY NONLINEAR SIMULATIONS

To explore the role of geometric and physical parameters in determining the disk falling styles, we solve the fully nonlinear system (1) starting from rest and letting time run

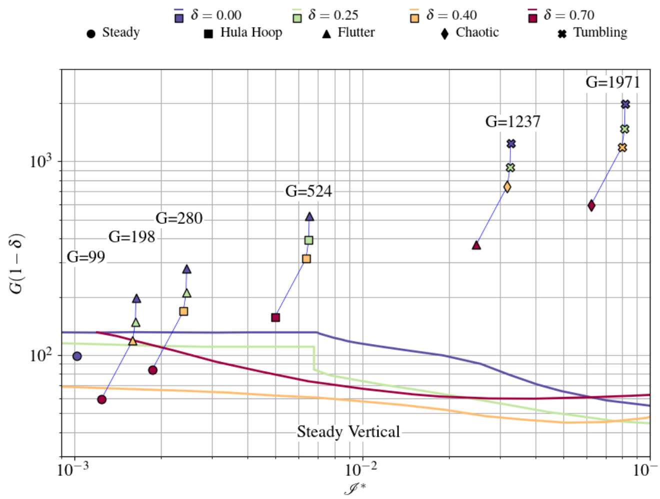

FIG. 11. (a) Falling styles [different symbols, see also Fig. 1(b)] from simulations of the fully nonlinear dynamics and marginal instability thresholds for steady vertical fall in the $(\mathscr{I}^*, G(1-\delta))$ plane $(\varepsilon = 1/60)$.

until a recognizable falling style is reached. Details on the numerical method are given in Appendix B.

In the following, we focus on the case $\varepsilon = 1/60$ and we compare the results of nonlinear dynamics with the marginal stability curves obtained for the same value of the thickness-to-diameter ratio. Following Tchoufag *et al.* [12], for a disk with external diameter D and a solid-fluid density ratio ρ_s/ρ, we introduce the Galileo number G defined as

$$G = \frac{DU_{\text{app}}}{\nu} = \frac{\sqrt{2|\rho_s/\rho - 1|g\varepsilon D^3}}{\nu}, \quad U_{\text{app}} = \sqrt{2|(\rho_s/\rho) - 1|g\varepsilon D}. \tag{10}$$

G is thus the Reynolds number based on U_{app}, an approximation of the nominal terminal velocity U_g obtained by setting $C_D = 1$ for the drag coefficient C_D when balancing weight and drag. In dimensional form, this balance reads

$$|\rho_s - \rho|g\varepsilon D^3(1-\delta^2)\pi/4 = \rho C_D D^2(1-\delta^2)U^2\pi/8; \tag{11}$$

U_g is the value of U obtained by solving (11) (this requires knowledge of C_D), while U_{app} is the value of U obtained by solving (11) with $C_D = 1$ (this only involves *a priori* known values of geometric and physical parameters). Therefore, the Galileo number provides a convenient parameter to classify the falling regime, since it does not require knowledge of aerodynamic properties, and it is independent of δ. Once the relation $C_D(\text{Re}, \delta)$ is known, the actual value for the Reynolds number (and thus of the nominal terminal velocity) is computed starting from G through the exact balance between drag and gravity, defined implicitly by

$$G^2 = \text{Re}^2 C_D(\text{Re}, \delta). \tag{12}$$

Vice versa, (12) can be used to attribute a Galileo number G to a disk for which the nominal terminal velocity U_g (hence Re) and δ are known. We remark that, at least in the parameter range we explore, the function $C_D(\text{Re})$ for fixed δ is monotonically increasing with respect to Re (see the Supplemental Material [36]), thus ensuring a unique solution.

We consider cases $G = 99, 198, 280, 524, 1237, 1971$ and inner holes with $\delta = 0, 0.25, 0.4, 0.7$. Following the rescaling employed by Vincent *et al.* [31], results of the nonlinear dynamics and stability analysis are represented together in the plane $(\mathscr{I}^*, (1-\delta)G)$. As concerns the marginal stability curves of Sec. IV, for given $\mathscr{I}^*$ and δ, we define $\text{Re}_{\text{cr}}(\mathscr{I}^*, \delta)$ as the smallest value of Re

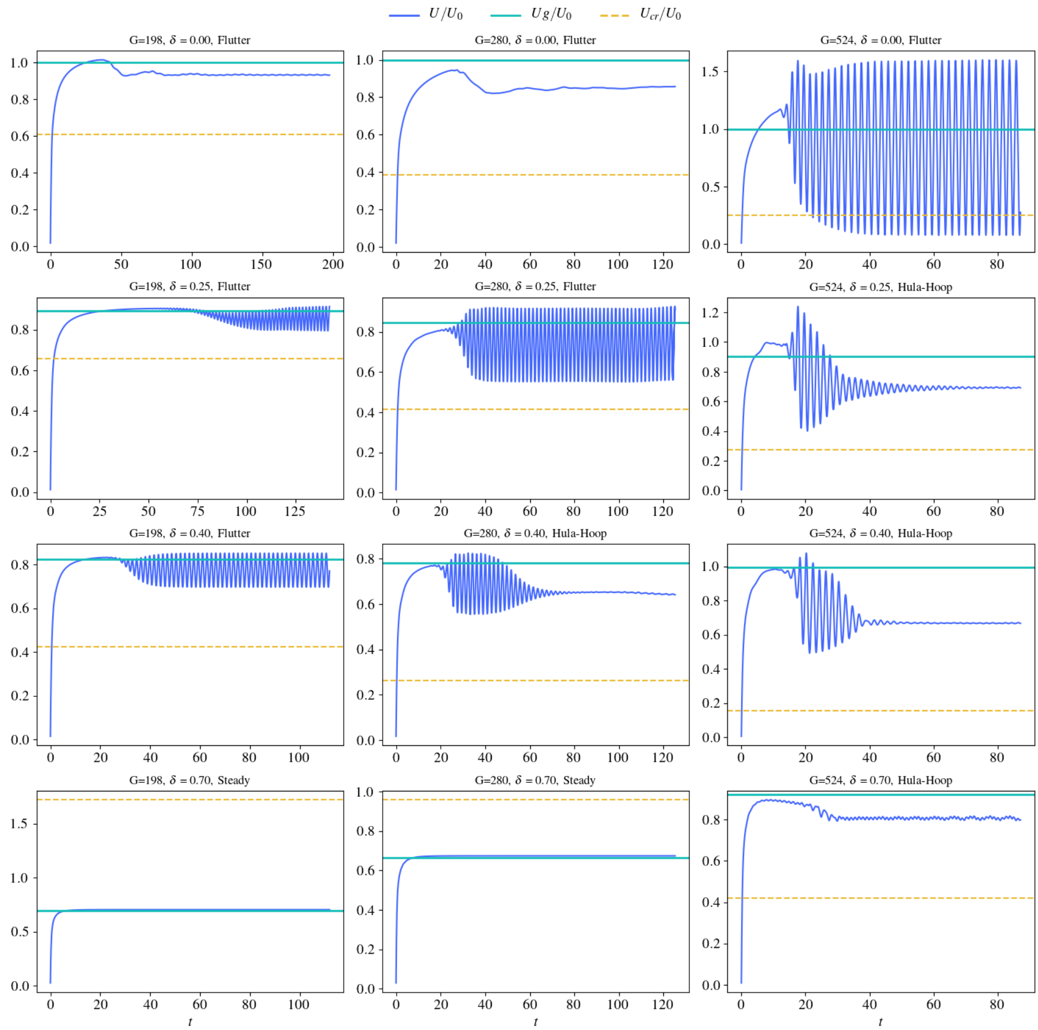

FIG. 12. Vertical velocity as a function of time, for different values of G and δ. For each value of G, velocities are rescaled with the nominal falling velocity of the full disk $U_0 = U_g(\delta = 0)$ ($\varepsilon = 1/60$).

beyond which the steady vertical path becomes unstable. We then compute the Galileo number of a disk with fixed δ through (12) and, in particular, $G_{cr}^2 = \mathrm{Re}_{cr}^2 C_D(\mathrm{Re}_{cr}, \delta)$ and transfer the marginal point in the $(\mathscr{I}^*, (1-\delta)G)$ plane, building a series of δ-dependent marginal curves. The points with coordinates $(\mathscr{I}^*, (1-\delta)G)$ are labeled as stable, hula-hoop, flutter, chaotic, or tumbling, according to the observed falling style. Figure 11 is thus interpreted as a phase diagram classifying the falling styles and providing a prediction of the critical stability conditions and of the observable nonlinear trajectories based only on intrinsic geometric and material parameters of the system.

In a free-falling numerical experiment starting from rest, the disk progressively accelerates, eventually leading to a constant terminal value or to oscillatory periodic/nonperiodic states. In terms of velocities, nonlinear simulations confirm that, if $G < G_{cr}$, a steady state is reached in a falling experiment starting from rest. The corresponding point $(\mathscr{I}^*, (1-\delta)G)$ lies below the marginal stability curve of the corresponding value of δ, in the region of the phase plane labeled as “stable.” Conversely, if $G > G_{cr}$, the steady fall mode becomes unstable before the nominal terminal value U_g is reached, and the corresponding point $(\mathscr{I}^*, (1-\delta)G)$ will lie beyond the stability curve.

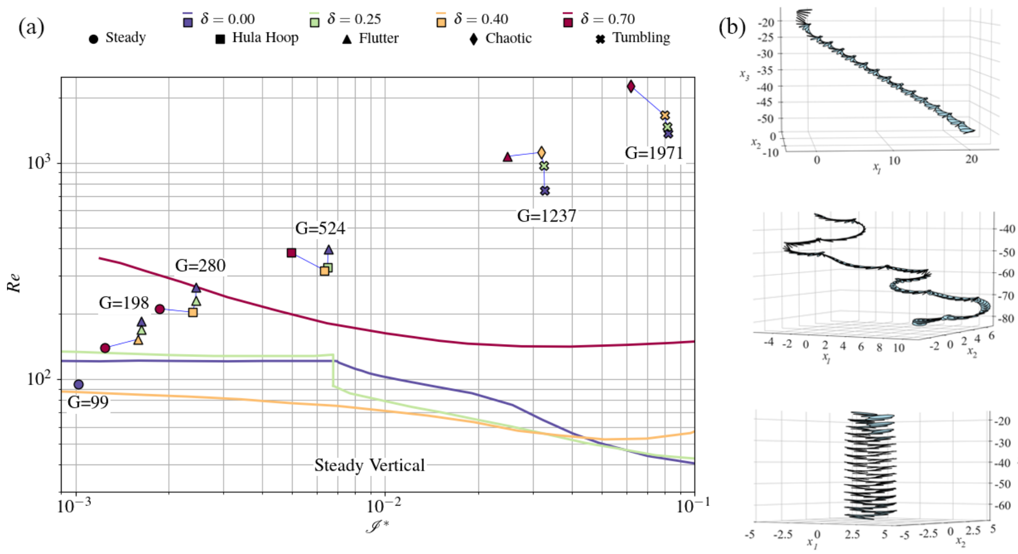

FIG. 13. (a) Falling styles from simulations of the fully nonlinear dynamics and curves marking the instability thresholds for steady vertical fall ($\varepsilon = 1/60$). (b) From the top to the bottom: tumbling: $G = 1971$, $\delta = 0$; chaotic motion: $G = 1237$, $\delta = 0.4$; flutter: $G = 524$, $\delta = 0$.

The plane $(\mathscr{I}^*, (1-\delta)G)$ can be subdivided into regions in which each of the falling styles is prevalent. Our simulations provide a few points in this phase diagram; see also the Supplemental Material for a comparison with the results of Auguste *et al.* [9] for full disks. Our results confirm and extend the ones obtained by Auguste *et al.* [9], to include larger values of Re and the effect of the hole size.

When the disk exhibits one of the unsteady but regular patterns, the following average velocity definition is employed: $U_{\mathrm{av}} = (2/T_f)\int_{T_f/2}^{T_f} \bar{v}_z(\bar{t})\mathrm{d}\bar{t}$, where $T_f/2$ is chosen as the time sufficient to reach a well-defined falling style, and T_f is the time at which the simulation is stopped. In general, U_{av} can be different from the nominal falling velocity U_g. Also, in the case of chaotic modes of descent, this quantity is not well-defined since the average velocities do not become independent of T. Data on instantaneous, terminal, and average falling velocity, normalized with $U_0 = U(\delta = 0)$, are reported in Fig. 12 for $G = 198, 280, 524$. For these values of G, opening a hole in a disk decreases the average fall velocity with respect to the case of the full disk. Also, average velocities computed in unsteady modes are smaller than the nominal velocity corresponding to the same value of material parameters. To visualize the dependence of the average velocity on material parameters in a compact way, Fig. 13 shows the results in the plane $(\mathscr{I}^*, \mathrm{Re})$. In opposition to Fig. 11, this diagram contains information about the actual average falling velocity, a quantity that is affected by the aerodynamic forces arising in the actual (possibly oscillatory) trajectory followed by the disk in its nonlinear dynamics. If the steady falling style is stable, $U_{\mathrm{av}} = U$ and the corresponding point is indeed below the $\mathrm{Re}_{\mathrm{cr}}$ curve, hence it is in the region of the phase diagram where the steady mode is stable. As observed in the $(\mathscr{I}^*, (1-\delta)G)$ plane, the results of numerical simulations agree well with the marginal stability boundary, showing a steady vertical path below the thresholds for the instability; see $G = 198$ and $\delta = 0.7$, and $G = 280$ and $\delta = 0.7$. In terms of falling styles, the graph confirms the observation by Vincent *et al.* [31] that opening a hole shifts the observed falling style according to the hierarchy: tumbling → chaotic → flutter → hula-hoop → steady, i.e., towards trajectories with smaller lateral dispersion and closer to the straight vertical one. As concerns the average falling velocity, points corresponding to G up to 524 show again that opening a hole decreases the average falling velocity with respect to the full disk.

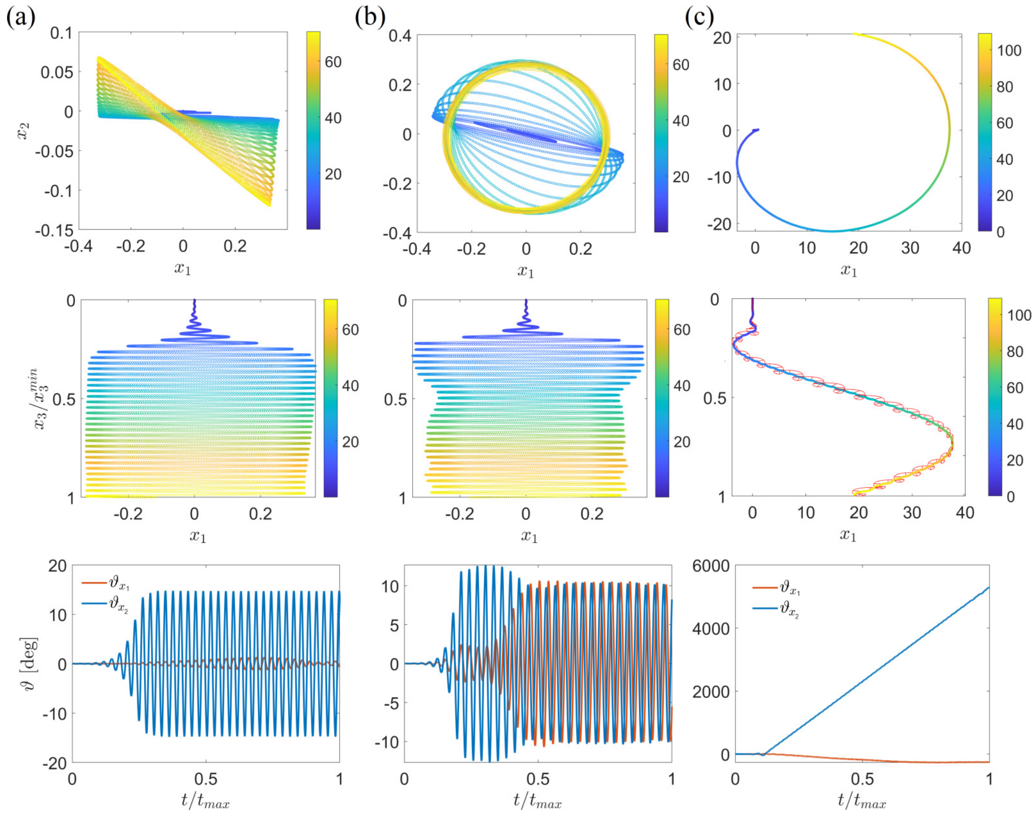

FIG. 14. Trajectories described in the absolute reference frame as functions of time, following the colormap (on the top and on the center), and unwrapped inclination angles ϑ_{x1} and ϑ_{x2} around the fixed axes as functions of time rescaled with its maximum value (on the bottom). $G = 280$ and (a) $\delta = 0.25$ (flutter), (b) $\delta = 0.4$ (hula-hoop); (c) $G = 1237$ and $\delta = 0$ (tumbling). The red line in panel (c) visualizes the normal-to-the-disk direction and helps in identifying the rotating motion of the disk in the tumbling regime.

This effect is similar to the slowing down of natural seeds granted by bristles and by hairy or porous structures [14]. Remarkably, this is no longer true for larger values of G explored here. In this regime ($G = 1237$, 1971), the full disks exhibit a tumbling motion, and opening a hole leads to a transition towards chaotic and fluttering falling styles, with higher average falling speed.

Figures 14(a) and 14(b) show the transition from a fluttering to a well-defined hula-hoop [9] as the hole size is increased. Hula-hoop patterns of annular disks have been recently observed in experiments by Zhang *et al.* [39]. In the fluttering case, the inclination angle variation occurs only around one direction [x_2, panel (a)], while hula-hoop motions are characterized by inclinations of the same amplitude, in the horizontal plane. During the tumbling trajectory, observed for a full disk at large G in Fig. 14(c), the disk mainly rotates around the x_2 axis, as shown by the trajectory and by the unwrapped angle. The chaotic motion shown in Fig. 13(b) appears as a random succession of regular falling patterns, i.e., flutter, tumbling, and hula-hoop motions. Analogous falling trajectories are observed for the other cases denoted as chaotic. Therefore, we can infer that chaotic motion seems to occur as a result of mode interactions that, taken individually, would lead to regular trajectories.

For thin disks, the presence of a central hole affects the free-fall nonlinear behavior in several ways. As general trends, we highlight the following ones. The opening of a hole in a full disk may promote more stable over less stable modes in the hierarchy of falling styles, namely modes of descent with trajectories that are closer to the steady vertical one and characterized by smaller lateral distance coverage (i.e., from tumbling to a chaotic mode of descent, from chaotic to fluttering, from fluttering to hula-hoop, and from hula-hoop to steady), as observed experimentally by Vincent *et al.* [31]. Up to moderate Galileo numbers (G up to 524 in our simulations), opening a hole leads to lower average fall velocities. At higher Galileo numbers ($G = 1237$, 1971), disks with holes fall at a higher average velocity than the corresponding full disk.

VI. CONCLUSIONS

In this paper, we performed a systematic study on the stability and falling trajectories of annular disks. We first considered the steady and axisymmetric vertical path and its stability with respect to azimuthal perturbations. The relative flow is characterized by a recirculation region which progressively detaches from the body, moves downstream, and disappears as the hole becomes larger. However, the separation at the disk's internal and external edges always leads to the formation of local recirculations. The drag exhibits a maximum at intermediate hole sizes, in analogy with permeable bodies. The existence of secondary recirculations attached to the edges of the disk modifies the picture observed in permeable cases, i.e., a destabilization-stabilization mechanism with increasing Re [26]. The region of stability of the vertical steady fall is, with a good approximation, a band occupying one side of the (Re, $\mathscr{I}^*$) plane. An increase in the hole size leads to a counterintuitive decrease of the marginal stability threshold at low inertia. However, for large-enough holes, the critical Reynolds number for the instability abruptly increases. Nonlinear simulations confirmed the observed behaviors in terms of neutral stability boundary and emerging patterns in the vicinity of the marginal stability thresholds. Besides, the hole promotes a transition in the hierarchy of falling modes, from tumbling to fluttering and hula-hoop motions. In particular, the departure from tumbling motions reduces by two orders of magnitude the horizontal distances reached by the disk. In summary, a central hole promotes the emergence of trajectories characterized by small deviations from the vertical one. At the same time, neutral curves present a nonmonotonous behavior, at low inertia. Therefore, an increase in the hole size does not always lead to the stabilization to a steady vertical path, based on the marginal stability curves of a full disk. The stabilization of the vertical path occurs only for very large holes. In analogy with the behavior of falling permeable bodies, a hierarchy in the modes stabilization is identified: the opening of a hole initially stabilizes modes and trajectories characterized by a dominance of wake oscillations over trajectory ones. Only for very large holes are modes with a dynamics dominated by the disk's degrees of freedom also stabilized.

In spite of the rich and diverse dynamics emerging from our study, some general trends emerge that may be useful for applications, e.g., the release by drones of biodegradable environmental sensors inspired by the dispersal strategies of natural seeds envisaged in Refs. [2,3]. Up to moderate G, opening a hole slows down descent speed and leads to a transition from flutter towards descent modes with trajectories closer to the straight vertical one. For large G, opening a hole leads to higher descent velocity and to a transition from tumbling towards fluttering descent modes, characterized by a smaller traveled lateral distance. The first regime (small G) may be of interest for controlled positioning on the ground, with seeds landing directly below the location of release from the drone. To avoid lateral dispersion caused by lateral winds, the release of individual seeds from small altitudes may be the optimal strategy. In this scenario, opening a hole may lead to better performance (straighter path) with respect to the case of a full disk. The second regime (large G) may be of interest for the release of several seeds from a single location at higher altitudes, aiming at large lateral distance covered. In this case, the tumbling trajectory is of greatest interest. Lower average falling speeds may also be beneficial, leading to larger lateral distance covered in the presence of lateral winds. Therefore, in this scenario, the full disk guarantees better performance than its perforated counterpart.

This work may find several extensions in the understanding of trajectories of falling objects and the selection of modes and trajectories through tailored shapes, e.g., nonplanar objects such as curved plates or cones, or bio-inspired shapes such as those of helicopter seeds. The approach

TABLE I. Variation of the nondimensional drag D_0 and of the real and imaginary parts of the almost marginally stable mode for $\varepsilon = 0.001$, $\delta = 0.3$, $\mathscr{I}^* = 0.0001$, Re = 106. From the left to the right: axial position of the inlet, axial position of the outlet, lateral boundary radial location, number of elements, drag, real part of the almost marginally stable mode, imaginary part of the almost marginally stable mode.

Mesh	Inlet ($x_{-\infty}$)	Outlet ($x_{+\infty}$)	Radius (r_∞)	N. Elem.	D_0	Re(σ)	Im(σ)
A	−25	50	25	26114	0.5354	0.00161	2.0462
B	−35	50	25	29131	0.5355	0.00101	2.0466
C	−40	50	25	30412	0.5354	0.00132	2.0463
D	−25	70	25	32049	0.5354	0.00127	2.0465
E	−25	100	25	40839	0.5357	0.00090	2.0471
F	−25	50	30	29734	0.5354	0.00131	2.0464
G	−25	50	40	36646	0.5354	0.00127	2.0465
H	−25	50	25	41345	0.5356	0.00093	2.0468
I	−25	50	25	82393	0.5355	0.00086	2.0468

advocated here, based on the synergistic use of linear stability analysis and nonlinear dynamics methods in the understanding of falling trajectories of annular disks in a large range of disk inertia, could be generalized in order to help better characterize falling trajectories of a large variety of objects with complex geometry.

ACKNOWLEDGMENTS

This work has received funding from the European Union's Horizon 2020 Research and Innovation Programme under Grant Agreement No. 101017940 (I-Seed). G.C.'s work was supported by #NEXTGENERATIONEU (NGEU) and funded by the Ministry of University and Research (MUR), National Recovery and Resilience Plan (NRRP), project THE (IECS00000017)—Tuscany Health Ecosystem (DN. 1553 11.10.2022). For the availability of high-performance computing resources and support, we acknowledge EuroHPC Joint Undertaking for awarding us access to LUMI at CSC, Finland (Proposal No. EHPC-DEV-2023D06-027), and we acknowledge the CINECA award under the ISCRA initiative, for the availability of high-performance computing resources and support (B Grant No. MT-SWS21).

APPENDIX A: GRID INDEPENDENCE ANALYSIS OF THE BASE FLOW AND STABILITY COMPUTATIONS

The mesh refinements are built in an analogous way to those of Ciuti *et al.* [17], except in the vicinity of the disk where a boundary layer refinement of size 0.1ε is employed, for Mesh A. Table I shows the sensitivity of the obtained results with respect to the position of the boundaries and to uniform refinements of the entire mesh. We verify the grid independence of drag and the results of the fluid-solid coupled eigenvalue problem in terms of the leading eigenvalue for the considered configuration. We move upstream of the inlet position. Subsequently, we verify the downstream position of the outlet and the radial location of the lateral boundary. In all calculations, three significant digits of the drag and of the leading eigenvalue remain constant. Further mesh refinements show that the real part varies from 0.00161 to 0.00086 when increasing the number of elements by a factor 3. However, this difference would not affect the main conclusion of this work since it leads to a variation of the critical Reynolds number below 1, which is the maximum accuracy of the performed stability computations. As a matter of fact, instability thresholds are obtained by linear interpolation of the eigenvalues between two successive integer values of Re when a change of sign of the real part is detected. Thus, Mesh A appears as a reasonable compromise between accuracy and computational times for the large number of stability computations (beyond 1000) required to explore the parameters space and to draw the neutral curves. Therefore, Mesh A is employed for all calculations of the base flow and stability analysis (Secs. III, IV, and the Supplemental Material).

APPENDIX B: VALIDATION OF THE NONLINEAR SOLVER

In Sec. V, Eq. (1) is solved numerically through a numerical implementation based on the one developed by Corsi and Lolli (see also [40]), designed to run on high performance computing platforms. The coupled system of equations (system of PDEs for the fluid and system of ODEs for the solid) is solved following the approach described by Mougin *et al.* [41], also used by Jenny *et al.* [7], with small variations. It is based on correcting the Kirchhoff equations, which describe the motion of a rigid body in an inviscid fluid, to take into account the effects of viscosity, and model the case of a fluid governed by the Navier-Stokes equations. The procedure was implemented in a finite-element code, which was validated against two benchmarks from the literature, detailed below. The incompressible Navier-Stokes equations are formulated on a moving domain, which follows the body during its rigid motion. The solution technique is standard: the pressure-velocity coupling is obtained with a projection method of the *Chorin* kind, i.e., the pressure is treated explicitly and the velocity field is solved for, then the pressure is corrected by enforcing the divergence-free constraint, the so-called *rotational incremental pressure-correction scheme* [42]. The solver is implemented within the framework of the open source Navier-Stokes solver *Oasis* [43], which in turn is based on the *FEniCS* [44] finite-element library. A standard projection scheme is already implemented in the *Oasis* library. The solver is modified by adding the terms related to apparent forces [see Eq. (1)], and to the moving domain, to the Navier-Stokes equations. The solution of the coupling with the solid also requires some further modifications. The equations are solved with a segregated approach, each component separately, in order to lower the computational effort. The viscous term is treated implicitly in time to ensure stability, while for the nonlinear convection term a second-order extrapolation is employed, i.e., $\mathbf{u}^n_{\text{conv}} = 2\mathbf{u}^{n-1} - \mathbf{u}^{n-2}$ (to which the relative velocity due to rigid body motion is subtracted), while the convective term is treated implicitly to avoid too strict time-step limitations due to the CFL number condition. As concerns the spatial discretization, Taylor-Hood $\mathbb{P}2/\mathbb{P}1$ finite elements are employed. Standard iterative Krylov solvers, from the linear algebra library *PETSc*, are exploited for the solution of the algebraic systems resulting from the discretization of the Navier-Stokes equations. More precisely, for the solution of the velocity problem, a *BiCGSTAB* solver, with *jacobi* preconditioner, is employed. For the pressure problem instead, the solver is *GMRES* with *AMG* multigrid preconditioner. The system of ODEs associated with (1) is advanced in time with the *SciPy* ODE integration routine *solve_ivp*. In the applications considered in this work, the Reynolds number, based on the average falling velocity of the disk, is at most of order of magnitude 10^3. Therefore, the flow surrounding the body might be in the transitional turbulent regime. In these cases, we employ an *LES* turbulence model. Specifically, we employ a *Smagorinsky-Lilly* model, already implemented in *Oasis* and validated against a benchmark case of transitional flow in Ref. [45]. The cases simulated entail a quiescent fluid in an unbounded domain. The domain is moving and follows the rigid body motion. Thus, the boundary of the computational mesh is spherical. The center of mass of the body is set to be at the origin of the sphere. The domain is large enough so that the wake that develops past the body is undisturbed; we set its diameter to 40 times the characteristic dimension of the solid (i.e., the diameter in the case of a disk). The mesh is composed of unstructured tetrahedra and generated with the *gmsh* utility [46]. The typical element count is of order 10^6. At the disk's surface, we employ boundary layers to ensure a constant cell size of $0.01D$. We check that the mesh is fine enough that the results are not affected by the element size.

To validate the solver, we first compare our implementation with the benchmark problem of the motion of a sphere in an unbounded domain [7]. A very similar case was considered in [47]. The flow is entirely determined by two control parameters: the ratio of solid to fluid density $\rho_r = \rho_s/\rho_f$

TABLE II. Results for the buoyancy-driven sphere benchmark. Galileo number $G_{\text{sph}} = 200$. Values from our simulations reported in the first row, errors relative to benchmark data in the last row.

	Horizontal velocity amplitude	Oscillation period
Simulations	0.241	31.0
Benchmark	0.2299	29.456
Error	4.7%	5.2%

and the Galileo number, which is defined as

$$G_{\text{sph}} = \frac{\sqrt{|\rho_r - 1|gD^3}}{\nu}, \tag{B1}$$

where g is the magnitude of the gravity vector, and D is the diameter of the sphere. Increasing the Galileo number results in a stronger interaction of the object with its own wake, and possible unsteadiness and/or loss of symmetry in the flow. The aim is to reproduce the case for $G_{\text{sph}} = 200$ and $\rho_r = 0.5$. In this case, the sphere is expected to undergo a periodic zigzagging motion. Following [47], we assign as an initial condition a small perturbation in order to trigger the instability of the wake. Then, the horizontal velocity magnitude and oscillation period are compared against those reported in the benchmark [7], nondimensionalized with the reference scales $U_{\text{ref}} = \sqrt{|\rho_r - 1|gd}$ and $t_{\text{ref}} = l_{\text{ref}}/U_{\text{ref}} = d/U_{\text{ref}}$, obtained by averaging over several periods of the oscillation.

A periodic zigzagging state is indeed reached after the initial transient. The comparison is reported in Table II. Results agree well with the benchmark case, with small discrepancies that can be imputed to differences between the meshes, time step, numerical tolerances, and methods employed in the present (finite elements) and the benchmark work (spectral elements).

For a second benchmark we consider the case of a disk. The case we consider has been studied by several authors [9,48,49], with different definitions of controlling parameters. We compare the results quantitatively with those reported in [48], and therefore we choose as controlling parameters $G_{\text{disk}} = 160$, $\rho_r = 0.99$, and $\varepsilon = 0.5$. It should be noted that here the reference velocity, also used in the calculation of the Galileo number, is defined as $U_{\text{ref}} = \sqrt{|\rho_r - 1|V^* gD}$, where $V^* = \frac{\pi}{4}\varepsilon$. The disk, released from an initial state of rest, will start ascending and develop a wake. Then, interaction with the wake causes an oscillatory motion, which is reported in all three of the cited studies. In our numerical test, we also observe that the motion sets to a periodic oscillation. We compare some numerical results with those in [48], as shown in Table III: the values compared are the Reynolds number, defined as $\text{Re} = U_m d/\nu$, with U_m average rising velocity, the normalized amplitude of the lateral component of velocity, AU_h/d, and the frequency of oscillation of the lateral motion, identified with the Strouhal number $\text{St} = fd/U_m$. The table shows that all values agree very well with those reported in the literature.

TABLE III. Results for the freely rising disk benchmark. Case for Galileo number $G = 160$. Data from our simulations reported in the first row, and compared with [48]. Errors relative to benchmark data in the last row.

	Re	AU_h/d	St
Simulations	244.56	0.246	0.108
Benchmark	241.73	0.237	0.107
Error	1%	4%	1%

[1] P. Ern, F. Risso, D. Fabre, and J. Magnaudet, Wake-induced oscillatory paths of bodies freely rising or falling in fluids, Annu. Rev. Fluid Mech. **44**, 97 (2012).
[2] B. Mazzolai, T. Kraus, N. Pirrone, L. Kooistra, A. De Simone, A. Cottin, and L. Margheri, Towards new frontiers for distributed environmental monitoring based on an ecosystem of plant seed-like soft robots, in *Proceedings of the Conference on Information Technology for Social Good* (ACM, New York, 2021), pp. 221–224.
[3] B. Mazzolai, T. Kraus, N. Pirrone, L. Kooistra, A. De Simone, A. Cottin, and L. Margheri, Advancing environmental intelligence through novel approaches in soft bioinspired robotics and allied technologies: I-seed project position paper for environmental intelligence in europe, in *Proceedings of the 2022 ACM Conference on Information Technology for Social Good* (ACM, New York, 2022), pp. 265–268.
[4] A. Belmonte, H. Eisenberg, and E. Moses, From flutter to tumble: inertial drag and Froude similarity in falling paper, Phys. Rev. Lett. **81**, 345 (1998).
[5] U. Pesavento and Z. J. Wang, Falling paper: Navier-stokes solutions, model of fluid forces, and center of mass elevation, Phys. Rev. Lett. **93**, 144501 (2004).
[6] A. Andersen, U. Pesavento, and Z. J. Wang, Analysis of transitions between fluttering, tumbling and steady descent of falling cards, J. Fluid Mech. **541**, 91 (2005).
[7] M. Jenny, J. Dušek, and G. Bouchet, Instabilities and transition of a sphere falling or ascending freely in a newtonian fluid, J. Fluid Mech. **508**, 201 (1999).
[8] S. Field, M. Klaus, M. Moore, and F. Nori, Chaotic dynamics of falling disks, Nature (London) **388**, 252 (1997).
[9] F. Auguste, J. Magnaudet, and D. Fabre, Falling styles of disks, J. Fluid Mech. **719**, 388 (2013).
[10] D. Fabre, P. Assemat, and J. Magnaudet, A quasi-static approach to the stability of the path of heavy bodies falling within a viscous fluid, J. Fluids Struct. **27**, 758 (2011).
[11] P. Assemat, D. Fabre, and J. Magnaudet, The onset of unsteadiness of two-dimensional bodies falling or rising freely in a viscous fluid: a linear study, J. Fluid Mech. **690**, 173 (2012).
[12] J. Tchoufag, D. Fabre, and J. Magnaudet, Global linear stability analysis of the wake and path of buoyancy-driven disks and thin cylinders, J. Fluid Mech. **740**, 278 (2014).
[13] C. Cummins, I. M. Viola, E. Mastropaolo, and N. Nakayama, The effect of permeability on the flow past permeable disks at low Reynolds numbers, Phys. Fluids **29**, 097103 (2017).
[14] C. Cummins, M. Seale, A. Macente, D. Certini, E. Mastropaolo, I. Viola, and N. Nakayama, A separated vortex ring underlies the flight of the dandelion, Nature (London) **562**, 414 (2018).
[15] P. G. Ledda, L. Siconolfi, F. Viola, F. Gallaire, and S. Camarri, Suppression of von Kármán vortex streets past porous rectangular cylinders, Phys. Rev. Fluids **3**, 103901 (2018).
[16] E. F. Strong, M. Pezzulla, F. Gallaire, P. Reis, and L. Siconolfi, Hydrodynamic loading of perforated disks in creeping flows, Phys. Rev. Fluids **4**, 084101 (2019).
[17] M. Ciuti, G. A. Zampogna, F. Gallaire, S. Camarri, and P. G. Ledda, On the effect of a penetrating recirculation region on the bifurcations of the flow past a permeable sphere, Phys. Fluids **33**, 124103 (2021).
[18] T. Tang, P. Yu, X. Shan, and H. Chen, The formation mechanism of recirculating wake for steady flow through and around arrays of cylinders, Phys. Fluids **31**, 043607 (2019).
[19] T. Tang, P. Yu, X. Shan, J. Li, and S. Yu, On the transition behavior of laminar flow through and around a multi-cylinder array, Phys. Fluids **32**, 013601 (2020).
[20] T. Tang, J. Xie, S. Yu, J. Li, and P. Yu, Effect of aspect ratio on flow through and around a porous disk, Phys. Rev. Fluids **6**, 074101 (2021).
[21] W. Zhang, D. Bi, and Y. Wei, Falling styles of perforated disks, Int. J. Multiphase Flow **161**, 104401 (2023).
[22] I. P. Castro, Wake characteristics of two-dimensional perforated plates normal to an air-stream, J. Fluid Mech. **46**, 599 (1971).
[23] L. Zong and H. Nepf, Vortex development behind a finite porous obstruction in a channel, J. Fluid Mech. **691**, 368 (2012).

[24] P. G. Ledda, E. Boujo, S. Camarri, F. Gallaire, and G. Zampogna, Homogenization-based design of microstructured membranes: wake flows past permeable shells, J. Fluid Mech. **927**, A31 (2021).
[25] P. G. Ledda, L. Siconolfi, F. Viola, S. Camarri, and F. Gallaire, Flow dynamics of a dandelion pappus: A linear stability approach, Phys. Rev. Fluids **4**, 071901(R) (2019).
[26] G. Vagnoli, G. Zampogna, S. Camarri, F. Gallaire, and P. Ledda, Permeability sets the linear path instability of buoyancy-driven disks, J. Fluid Mech. **955**, A29 (2023).
[27] G. A. Zampogna and A. Bottaro, Fluid flow over and through a regular bundle of rigid fibres, J. Fluid Mech. **792**, 5 (2016).
[28] G. A. Zampogna, J. Magnaudet, and A. Bottaro, Generalized slip condition over rough surfaces, J. Fluid Mech. **858**, 407 (2019).
[29] G. Zampogna and F. Gallaire, Effective stress jump across membranes, J. Fluid Mech. **892**, A9 (2020).
[30] H. Moffatt, Three coins in a fountain, J. Fluid Mech. **720**, 1 (2013).
[31] L. Vincent, W. S. Shambaugh, and E. Kanso, Holes stabilize freely falling coins, J. Fluid Mech. **801**, 250 (2016).
[32] W. Zhou and J. Dušek, Chaotic states and order in the chaos of the paths of freely falling and ascending spheres, Int. J. Multiphase Flow **75**, 205 (2015).
[33] D. Bi, Y. Wei, R. Theunissen, and H. Xu, Study on the flow structure behind a freely falling annular disk using proper orthogonal decomposition, Eur. J. Mech. B: Fluids **85**, 90 (2021).
[34] D. Bi, T. Sun, Y. Wei, and X. Huang, On the dynamic behaviors of freely falling annular disks at different Reynolds numbers, Phys. Fluids **34**, 043307 (2022).
[35] P. Meliga, J.-M. Chomaz, and D. Sipp, Unsteadiness in the wake of disks and spheres: instability, receptivity and control using direct and adjoint global stability analyses, J. Fluids Struct. **25**, 601 (2009).
[36] See Supplemental Material at http://link.aps.org/supplemental/10.1103/PhysRevFluids.9.043907 for additional results and details, which include Refs. [9,15,17,26,35,50,51].
[37] D. Fabre, F. Auguste, and J. Magnaudet, Bifurcations and symmetry breaking in the wake of axisymmetric bodies, Phys. Fluids **20**, 051702 (2008).
[38] P. Meliga, J.-M. Chomaz, and D. Sipp, Global mode interaction and pattern selection in the wake of a disk: a weakly nonlinear expansion, J. Fluid Mech. **633**, 159 (2009).
[39] W. Zhang, D. Bi, and Y. Wei, Effect of porosity on the kinematics of free-falling porous disks, Phys. Fluids **35**, 013604 (2023).
[40] A. Lolli, G. Corsi, and A. De Simone, Control and navigation problems for model bio-inspired microswimmers, Meccanica **57**, 2431 (2022).
[41] G. Mougin and J. Magnaudet, Path instability of a rising bubble, Phys. Rev. Lett. **88**, 014502 (2001).
[42] J.-L. Guermond, P. Minev, and J. Shen, An overview of projection methods for incompressible flows, Comput. Methods Appl. Mech. Eng. **195**, 6011 (2006).
[43] M. Mortensen and K. Valen-Sendstad, Oasis: A high-level/high-performance open source Navier-Stokes solver, Comput. Phys. Commun. **188**, 177 (2015).
[44] M. Alnæs, J. Blechta, J. Hake, A. Johansson, B. Kehlet, A. Logg, C. Richardson, J. Ring, M. E. Rognes, and G. N. Wells, The FEniCS Project Version 1.5, Archive of Numerical Software **3**(100) (2015).
[45] J. Bø, A. Bergersen, K. Valen-Sendstad, and M. Mortensen, Implementation, verification and validation of large eddy simulation models in oasis, in *8th National Conference on Computational Mechanics MekIT'15*, edited by B. Skallerud and H. I. Andersson (CIMNE, Barcelona, 2015), pp. 99–122.
[46] C. Geuzaine and J.-F. Remacle, Gmsh: A 3-d finite element mesh generator with built-in pre-and post-processing facilities, Numer. Meth. Eng. **79**, 1309 (2009).
[47] F. Auguste and J. Magnaudet, Path oscillations and enhanced drag of light rising spheres, J. Fluid Mech. **841**, 228 (2018).
[48] M. Chrust, G. Bouchet, and J. Dušek, Effect of solid body degrees of freedom on the path instabilities of freely falling or rising flat cylinders, J. Fluids Struct. **47**, 55 (2014), special Issue on Unsteady Separation in Fluid-Structure Interaction-l.

[49] A. R. Shenoy and C. Kleinstreuer, Influence of aspect ratio on the dynamics of a freely moving circular disk, J. Fluid Mech. **653**, 463 (2010).

[50] P. Huerre and P. A. Monkewitz, Local and global instabilities in spatially developing flows, Annu. Rev. Fluid Mech. **22**, 473 (1990).

[51] F. Giannetti and P. Luchini, Structural sensitivity of the first instability of the cylinder wake, J. Fluid Mech. **581**, 167 (2007).